Inorganic Chemistry

pubs.acs.org/IC Article

Cage Adaption by High-Pressure Synthesis: The Clathrate-I Borosilicide $Rb_8B_8Si_{38}$

Julia-Maria Hübner,* Walter Jung, Marcus Schmidt, Matej Bobnar, Primož Koželj, Bodo Böhme, Michael Baitinger, Martin Etter, Yuri Grin, and Ulrich Schwarz

Cite This: *Inorg. Chem.* 2021, 60, 2160–2167 Read Online

ACCESS | Metrics & More | Article Recommendations | Supporting Information

ABSTRACT: $Rb_8B_8Si_{38}$ forms under high-pressure, high-temperature conditions at p = 8 GPa and T = 1273 K. The new compound (space group $Pm\bar{3}n$, a = 9.9583(1) Å) is the second example for a clathrate-I borosilicide. The phase is inert against strong acids and bases and thermally stable up to 1300 K at ambient pressure. $(Rb^+)_8(B^-)_8(Si^0)_{38}$ is electronically balanced, diamagnetic, and shows semiconducting behavior with moderate Seebeck coefficient below 300 K. Chemical bonding analysis by the electron localizability approach confirms the description of $Rb_8B_8Si_{38}$ as Zintl phase.

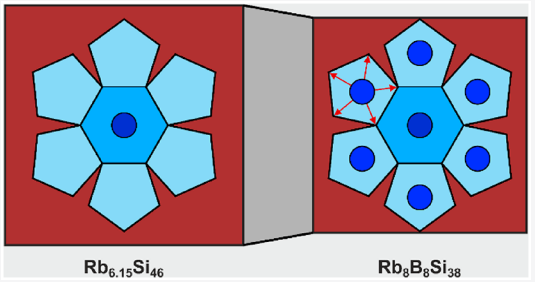

1. INTRODUCTION

Intermetallic boron compounds are often characterized by high thermal stability[1,2] and are thus frequently studied as candidate materials in application oriented research, e.g., in the context of thermoelectrics.[3−8] The often complex crystal structures provide a favorable basis for the required low heat conductivity, and a number of extensive studies focused on low-density binary and ternary borides.[4] More recent interest was directed on framework compounds of abundant elements such as boron-rich chalcogenides B_6X (X = S, Se), boron suboxide B_6O, or boron carbide.[5−8] Borosilicides with high boron content typically form framework structures comprising $[B_{12}]^{2-}$ dodecahedra.[1] In boron-rich compounds like $Li_2B_{12}Si_2$[9] or $Tb_{0.68}B_{12}Si_{3.04}$,[10] the dodecahedra are interconnected via exo-bonds or Si_2 dumbbells. In $Na_8B_{74.5}Si_{17.5}$, multicenter bonds in closo-clusters go along with four-bonded silicon atoms interconnecting the clusters.[11]

By comparison, silicon-rich borosilicides are rare. One of the few examples is clathrate-I type $K_7B_7Si_{39}$, comprising four-bonded boron in the polyanion.[12] In contrast, most of the alkali metal silicon clathrates of the heavier homologues Al and Ga $A_{8-x}Z_{8-y}Si_{38+y}$ (A = Na, K, Rb, Cs, Z = Al, Ga with x < 0.55, y < 0.9) have already been prepared,[13−17] of which $Na_8Al_8Si_{38}$, $K_8Al_8Si_{38}$, $Rb_8Al_8Si_{38}$, and $Rb_8Ga_8Si_{38}$ adopt nonmetal-deficient and electron-precise compositions in agreement with the Zintl rule. Nevertheless, subsequent attempts to prepare further boron-containing clathrate-I phases remained unsuccessful at ambient pressure. At this stage, the synthesis strategy was reconsidered by taking into account the beneficial effect of elevated pressures as evidenced by the recent preparation of the borosilicide $LiBSi_2$ comprising a $[Si_2B^-]_n$ framework of four-bonded atoms[18] and the theoretical prediction of quenchable sodalite-type RbB_3Si_3.[19]

In the scope of the present work, the influence of high-pressure conditions on the formation of a clathrate-I borosilicide is investigated. We find that high-pressure synthesis grants access to the clathrate-I $Rb_8B_8Si_{38}$ showing remarkable thermal stability. The adaption of the crystal structure to cage filling and boron substitution is discussed, and the chemical bonding is studied by quantum chemical methods in direct space. Finally, thermal and electronic transport properties are reported.

2. EXPERIMENTAL SECTION

Synthesis. Sample handling, except for high-pressure synthesis and washing procedure, was performed in argon-filled glove boxes (MBraun, H_2O and O_2 < 0.1 ppm). Rubidium (Chempur, 99.95%) and silicon (Chempur, 99.9999%) were used to synthesize the precursor compound $Rb_{12}Si_{17}$ in a closed tantalum tube by annealing at 750 °C for 7 h and slow cooling to room temperature within 8 h. Amorphous boron (Alfa Aesar) was cleaned and activated in a streaming hydrogen plasma.[20] High-pressure, high-temperature preparation started from educt mixtures with ratio Rb:B:Si = 3.25:2:5, which were thoroughly ground in agate mortars. The powders were filled into boron nitride crucibles before being placed in MgO octahedra with an edge length of 18 mm. The high-pressure, high-temperature syntheses were conducted using a multianvil press comprising a Walker-type module.[21] Calibration of pressure and temperature had been realized prior to the experiments by recording the resistance changes of bismuth and thermocouple-calibrated runs,

Received: August 10, 2020
Published: October 26, 2020

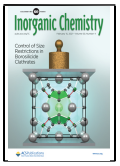

https://dx.doi.org/10.1021/acs.inorgchem.0c02357
Inorg. Chem. 2021, 60, 2160–2167

respectively. A pressure of p = 8 ± 1 GPa was applied, and the samples were heated to T = 1273 ± 127 K within 15 min. After annealing for 300 min, the samples were quenched under load. The reaction products were washed with ethanol and deionized water to remove traces of highly reactive Rb_4Si_4, followed by washing with ethanol and acetone and drying at room temperature. The compound is air stable and inert against strong acids and bases.

XRPD. Sample characterization was done with a Guinier camera (Huber G670, Cu$K\alpha_1$ radiation λ = 1.54056 Å, germanium monochromator, measurement range 5° ≤ 2θ ≤ 100°, $\Delta 2\theta$ = 0.005°). Rietveld refinements were performed using synchrotron data (Desy Hamburg, PETRA III, Beamline P02.1, λ = 0.20720 Å) recorded at room temperature. Reflection positions were corrected using LaB_6 standard (NIST), and unit cell parameters were calculated from least-squares refinement. Crystallographic calculations were performed with the *WinCSD* program package.[22]

Thermal Analysis. Thermogravimetry and differential thermal analysis was conducted simultaneously with a NETZSCH STA 449C device (Netzsch-Gerätebau GmbH, Selb, Germany) using a Knudsen cell made of tantalum and heating rates of 10 K min^{-1} under an argon atmosphere.

Metallography. Specimens were embedded in paraffin and polished with a suspension of diamond powders (grain sizes 6, 3, and 0.25 μm). Wavelength-dispersive X-ray spectroscopy (WDXS) was carried out with a Cameca SX100 electron microprobe equipped with a tungsten cathode. Ni_3B, Mg_2Si, and RbI were used as standards. The analysis comprehended intensity measurements of the B−Kα, Si−Kα, and Rb-Lα lines. The X-ray emission lines were excited at an electron beam of 7 keV and a beam current of 100.00(1) nA for B, 15 keV and 8.00(1) nA for Si, and 15 keV and 40.00(1) nA for Rb, respectively. The WDX spectrometer was equipped with LPC3, TAP, or LPET monochromator crystals.

NMR. Nuclear magnetic resonance (NMR) experiments were performed on a Bruker Avance 500 spectrometer with a magnetic field of B_0 = 11.74 T. The standard Bruker MAS probe for 2.5 mm ZrO_2 rotors was used for ^{29}Si experiments, whereas the static probe (NMR Service GmbH, Erfurt, Germany) was used for ^{11}B experiments. The ^{29}Si and ^{11}B signals were referenced to 1 vol % tetramethylsilane (TMS) and $BF_3 \times Et_2O$ with the reference frequencies of 99.3596 and 160.4588 MHz, respectively. In the case of ^{29}Si, the Hahn-echo sequence (90°−τ−180°−τ−acquisition) with a 90° pulse of 1.8 μs, interpulse delay of 100 μs and the recovery time of 5 s was applied. The MAS rotation rate was 30 or 29 kHz. For the ^{11}B spectra, the signal acquisition was achieved after a single pulse of 2.5 μs and recovery times of 30 s.

Electronic Structure Calculations and Chemical Bonding Analysis. For quantum chemical computations on $Rb_8B_8Si_{38}$, the mixed occupation of the 16*i* position in space group $Pm\bar{3}n$ was described by an ordered structure model in space group $P\bar{4}3n$ with boron and silicon each located on an 8*e* position. Moreover, the coordinate of the boron atoms 1/2 − x was optimized to a value of x = 0.1812 by total energy calculations being markedly different to x = 0.1912(2) for the averaged Si2/B2 position from X-ray structure refinements.

The electronic structure was calculated by means of the all-electron, full-potential local orbital (FPLO) method.[23] All results were obtained within the local density approximation (LDA) to the density functional theory using the Perdew−Wang parametrization for the exchange-correlation effects.[24] A mesh of 12 × 12 × 12 k points was used for calculations.

Chemical bonding analysis in position space was performed within the approach of combined topological analysis of electron density (ED) and electron localizability indicator (ELI). The analysis of the ED was made on the basis of the quantum theory of atoms in molecules (QTAIM).[25] ELI[26,27] was calculated in the ELI-D representation by a module implemented in FPLO.[28] The topological analysis of ED and ELI-D was carried out by the program *DGRID*.[29]

Transport Properties. Electrical resistivity, thermal conductivity, and Seebeck coefficient were measured simultaneously on a physical property measurement system with thermal transport option (PPMS, Quantum Design). $Rb_8B_8Si_{38}$ powder was cold pressed to a plate (2.6 × 1.4 × 0.25 mm^3) and contacted in a four-terminal configuration using flat gold-plated copper leads and silver epoxy (Epotek H20e). The uncertainty of resistivity and conductivity was estimated to amount to ±50% and that of the Seebeck coefficient to 25% because of uncertainties in sample geometry.

Magnetic Susceptibility. Powder samples were measured in open quartz tubes with a squid magnetometer (MPMS XL-7, Quantum Design) from 1.8 to 300 K in external fields between 0.2 mT and 7 T.

3. RESULTS AND DISCUSSION

The X-ray powder diffraction pattern of $Rb_8B_8Si_{38}$ (a = 9.9583(1) Å) reveals the clathrate-I-type crystal structure[30] with space group $Pm\bar{3}n$ (Figure 1 and Table S1). Rietveld

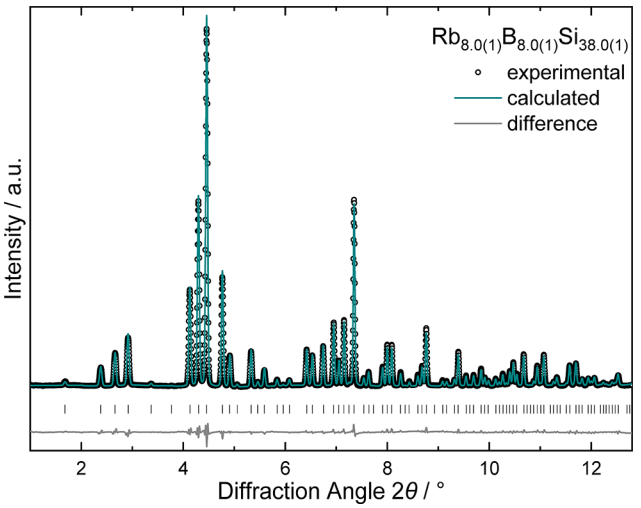

Figure 1. Powder X-ray diffraction pattern of $Rb_8B_8Si_{38}$ (synchrotron radiation, λ = 0.20709 Å) with the results of the crystal structure refinement.

refinements using binary Rb_8Si_{46-x} as a structure model show that the smaller 20-atom dodecahedral and the larger 24-atom tetrakaidecahedral cages are fully occupied by Rb1 (Wyckoff position 2*a*) and Rb2 (6*d*), respectively (Table 1 and Table S2 and Figure S1). In the framework, position Si1 (6*c*) is fully occupied by silicon atoms, whereas enlarged displacement parameters for Si2 on position 16*i* and Si3 on site 24*k* point to mixed B/Si occupancy. Indeed, position 16*i* shows a distinctly reduced electron density, which is compatible with the occupancy of 9.36(6) Si2 and 6.64 B atoms. The slightly decreased electron density at position 24*k* is assigned to a

Table 1. Atomic Coordinates and Displacement Parameters B_{eq}[a] (in Å^2) for $Rb_8B_8Si_{38}$ (space group $Pm\bar{3}n$, a = 9.9588(2) Å), for the Anisotropic Displacement Parameters see Table S2

atom	site	x	y	z	B_{eq}[a]
Rb1	2*a*	0	0	0	1.03(2)
Rb2	6*d*	0.25	0.5	0	1.43(3)
Si1	6*c*	0.25	0	0.5	1.39(7)
Si2/B[b]	16*i*	0.1912(2)	x	x	1.56(4)
Si3/B[c]	24*k*	0	0.2973(2)	0.1243(2)	1.43(5)

[a] B_{eq} = 1/3[$B_{11}a^{*2}a^2$ + ... 2 B_{23} b^*c^*bc cos α)]; Berar factor: 6.1. [b] $Si_{0.585(4)}B_{0.415}$. [c] $Si_{0.945(4)}B_{0.055}$.

https://dx.doi.org/10.1021/acs.inorgchem.0c02357
Inorg. Chem. 2021, 60, 2160−2167

mixture of 22.68(9) Si3 and 1.32 B atoms. The total number of boron atoms amounts to 7.96(15) per formula unit and equals, and thus, the alkali metal content within the estimated error. The final composition $Rb_8B_8Si_{38}$ is consistent with an electron-balanced Zintl phase. Composition analysis by wavelength-dispersive X-ray spectroscopy resulted in $Rb_{8.1(1)}B_{8.5(1)}Si_{37.4(1)}$ (normalized to 100%, this corresponds to $Rb_{15.0(1)}B_{15.8(1)}Si_{69.2(1)}$), which is in fair agreement with the composition refined in the diffraction experiment ($Rb_8B_8Si_{38}$) considering the known experimental limits in the quantitative analysis of light elements like boron.

The obtained powder diffraction data preclude the refinement of split atom positions.[12] Therefore, the short distance d(16*i*-16*i*) of 2.029(2) Å represents a mean value resulting from the superposition of d(Si2−Si2) and d(B−Si2). In a similar vein, d(16*i*-24*k*) = 2.277(2) Å resembles an average of Si−Si and Si−B distances. Contacts d(6*c*−24*k*) = 2.376(2) Å and d(24*k*−24*k*) = 2.475(2) Å appear as basically regular silicon−silicon distances d(Si1−Si3) and d(Si3−Si3), respectively, because of the low substitution level of position 24*k* (Si3) (Table S3). A peculiar feature of $Rb_8B_8Si_{38}$ (and also $K_7B_7Si_{39}$) is the predominant substitution of silicon atoms on position 16*i* (Si2). The site typically shows the shortest interatomic framework distances, e.g., in the related binary silicon clathrates $K_{8-x}Si_{46}$[31] or $Rb_{6.15}Si_{46}$[32,33] and is thus best suited for accommodating the small boron atoms. Position 6*c* (Si1),[34,35] which is preferred by larger substitution atoms like transition metals, is avoided by boron as the resulting local configuration and interatomic distances would be unfavorable for sp^3-hybridized boron atoms. The substitution of Si by the heavier homologues Al or Ga in $Rb_8Al_8Si_{38}$ and $Rb_8Ga_8Si_{38}$ affects all Si sites, although it appears predominantly at 6*c*.[14,16]

Comparison of lattice parameters (Figure 2, Table S3) reveals reduced values for ternary clathrate-I borosilicides[12] in relation to their binary analogs,[32,33,36−40] e.g., the unit cell of $Rb_8B_8Si_{38}$ (a = 9.9583(1) Å) is significantly smaller than that of $Rb_{6.15}Si_{46}$ (a = 10.27188(6) Å)[32,33] in which the dodecahedral cages are almost empty. The lattice parameter

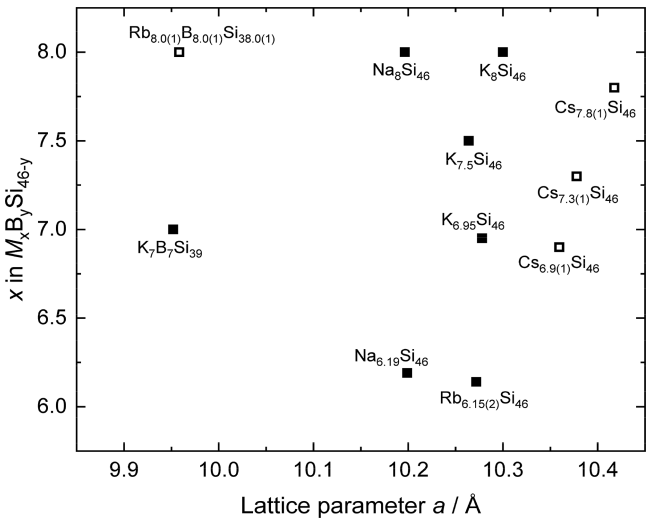

Figure 2. Lattice parameter vs cage filling level x for clathrate-I borosilicides $M_xB_ySi_{46-y}$ in comparison to binary clathrates M_xSi_{46} (M = Na, K, Rb, Cs). Full symbols indicate products synthesized at ambient pressure, open symbols denote high-pressure products. Experimental errors are smaller than the size of the symbols.

is connected to the framework contacts of position 16*i* and the metal-network distances in the small cages (Figure 3) by the relation

$$a\sqrt{3} = 2d(16i - 16i) + 4d(2a - 16i)$$

As boron substitution and rubidium defects mainly affect positions, which are located on the body diagonal of the unit cell, the shortening of the framework distances d(16*i*−16*i*) in the ternary phase (Table S3) goes along with a pronounced contraction of the lattice.

On the other hand, the value for the lattice parameter of $Rb_8B_8Si_{38}$ (a = 9.9583(1) Å) is strikingly similar to that of $K_7B_7Si_{39}$ (a = 9.952(1) Å)[12] in which half of the dodecahedral cages are empty. For describing the framework adaption to the larger rubidium atoms, a model is applied in which the metal-centered dodecahedra (yellow in Figure 4) are surrounded by Rb2 and Si1 atoms adopting Zeolite A topology.[41] The atoms of this 24-atom sodalite cage (gray in Figure 4) remain unaffected by boron substitution and alkali metal deficit. The edge length of the polyhedron, l = 1/4 $a\sqrt{2}$, directly scales with the lattice parameter because the metal (6*d*) and Si1 atoms (6*c*) occupy special positions without variable parameters. Because the lattice parameters of $K_7B_7Si_{39}$ and $Rb_8B_8Si_{38}$ are nearly identical, the sodalite cage adopts practically the same size in both crystal structures. Nevertheless, the size of the inner dodecahedral cage can still adapt to the radius of the metal atom. Replacement of potassium by the larger rubidium atoms goes along with longer distances between metal and framework and between Si3/B−Si3/B in the smaller 20-atom polyhedron (Figure 4). Simultaneously, distances Si2/B−Si2/B and, to a lesser extent, Si1−Si3/B become shorter (Table S3).

The local arrangement of boron and silicon atoms is characterized by solid-state NMR spectroscopy. The ^{11}B NMR spectrum shows a strong, slightly asymmetric signal centered at −25 ppm, and a weak signal at 60 ppm, agreeing with two boron positions as evidenced by the X-ray diffraction experiment (Figure 5). Boron pairs do not occur as the presence of [BSi_4] and [$BBSi_3$] entities in the tetrahedral framework would result in a more complex ^{11}B NMR spectrum. Therefore, only one out of two neighboring Si2 positions (site 16*i*) is substituted by boron atoms. The slight asymmetry of the stronger signal is attributed to the axial symmetry of the Si2 position and positional disorder. The ^{29}Si NMR spectrum shows a broad signal extending from −100 ppm to 600 ppm (Figure 5, inset), which is assigned to the superposition of different local configurations. Similar spectra have also been observed for other substituted silicon clathrates.[42] Absence of an NMR Knight shift indicates a low density of states at the Fermi level, which is in line with the electron-balanced composition obtained from structure refinement.

The topological features of the partially substituted and compressed clathrate-I framework motivate investigation of chemical bonding. For quantum chemical calculations, an ordered structure representation in space group $P\bar{4}3n$[43] models the disordered silicon and boron distribution in the framework of $Rb_8B_8Si_{38}$. The noncentrosymmetric subgroup allows for a transformation of the mixed occupied 16*i* position of space group $Pm\bar{3}n$ into two 8*e* positions in $P\bar{4}3n$, which are alternatively occupied by B and Si, respectively. The coordinates of the boron position are optimized by total energy calculations. In the calculated density of states (Figure

https://dx.doi.org/10.1021/acs.inorgchem.0c02357
Inorg. Chem. 2021, 60, 2160−2167

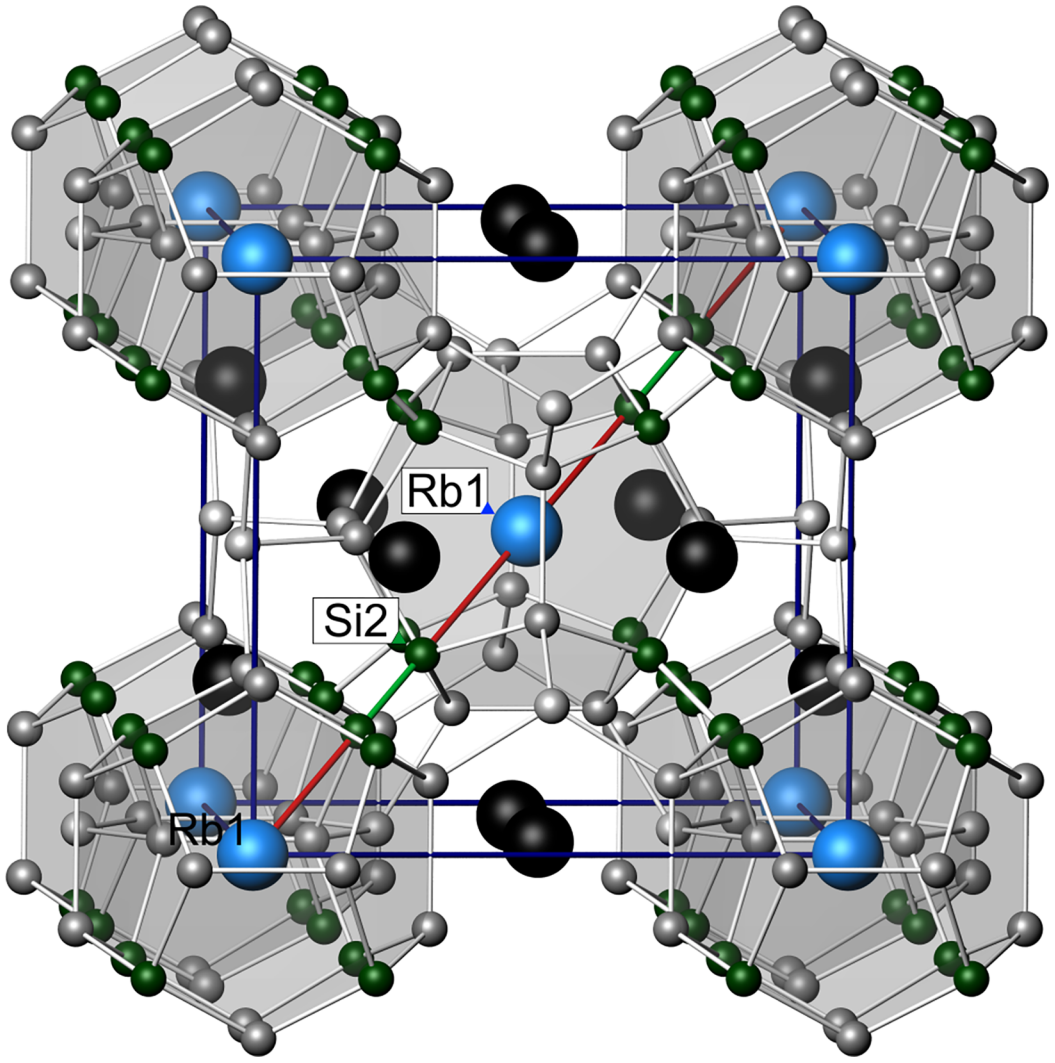

Figure 3. Clathrate-I arrangement with emphasis on the network of interconnected dodecahedral cages. Interatomic distances d(Rb1−Si2) (red) and d(Si2−Si2) (green) are oriented along the unit cell diagonal.

6) the range at low energies (<6 eV) is dominated by the s states of boron and silicon, whereas their p states are located in the region below the Fermi level, reflecting the bonding within the framework. Consistent with the charge transfer in the Zintl model, the s states of rubidium are empty and contribute to the density of states above the Fermi level.

The effective charges in $Rb_8B_8Si_{38}$ are analyzed within the Quantum Theory of Atoms in Molecules (Figure 7).[25] In accordance with the electronegativity values, the Rb atoms carry positive ($Rb1^{+0.68}$, $Rb2^{+0.76}$) and the B atoms negative charges (−0.72), whereas Si atoms exhibit values around zero (Figure 7, top). For comparison, the QTAIM charges for the hypothetical binary compound Rb_8Si_{46} using structure data[21] are $Rb1^{+0.59}$, $Rb2^{+0.57}$, $Si1^{-0.07}$, $Si2^{-0.09}$, and $Si3^{-0.12}$. Evidently, the presence of the more electronegative boron atoms in $Rb_8B_8Si_{38}$ induces a higher charge transfer from the rubidium atoms onto the framework. This finding is also in accordance with the smaller lattice parameter of the boron-substituted clathrate because of increased Coloumb interactions. With the boron atoms carrying a negative charge of −0.72 and effective charges of the silicon close to zero, the electron balance is in agreement with the Zintl model. However, the Coulomb contributions to the stabilization of the structure in the Rb compounds is less significant than in binary clathrates of Ba[44] or Sr[45] because of the lesser charge transfer.

Further confirmation of the Zintl-phase character of the new borosilicide is obtained from the distribution of the electron-localizability indicator (ELI-D; Figure 7 bottom). The spherical ELI-D distribution around the Rb nuclei and the absence of the last shell confirm charge transfer from the rubidium atoms to the framework. Each Si−Si and B−Si contact exhibits an ELI-D attractor, and the populations of the basins are close to two electrons. As these basins consist of Si and B contributions, the covalent two-atomic character of the Si−Si and Si−B bonds is evidenced.

TG/DTA measurements of $Rb_8B_8Si_{38}$ reveal thermal decomposition at 1305(10) K (Figure 8) plus a feature at 1130(5) K which is attributed to a side phase or recrystallization of the product. The mass loss is consistent with the evaporation of the Rb atoms, and the decomposition product only shows reflections of α-Si in XRPD. The high thermal stability, the balanced composition, and the complex crystal structure are preconditions for materials with potential thermoelectric properties.

The electrical resistivity of $Rb_8B_8Si_{38}$ with ρ(300 K) = 0.02 Ω m is in the range of doped α-Si or α-Ge[46] and shows a

https://dx.doi.org/10.1021/acs.inorgchem.0c02357
Inorg. Chem. 2021, 60, 2160−2167

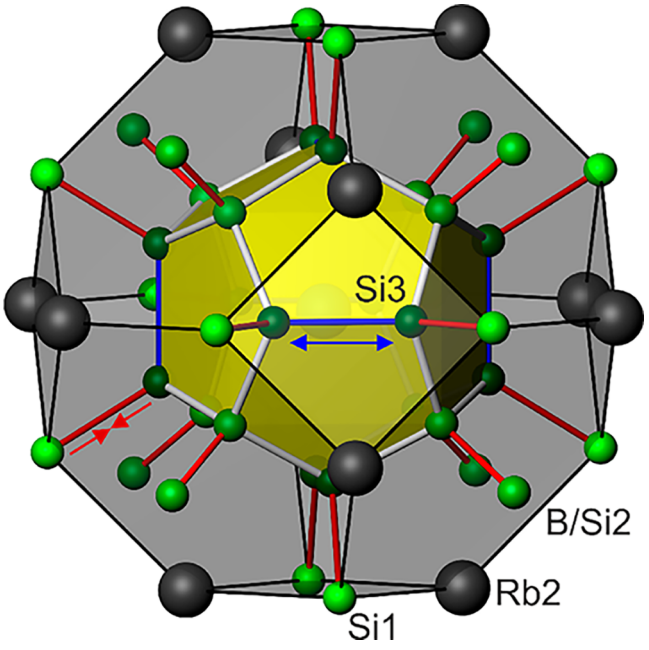

Figure 4. Adaption of the clathrate-I structure to framework substitution, cage filling and size of the filler atom. Increasing distances are denoted in blue, decreasing ones in red. The size of the sodalite cage (gray) scales with the lattice parameter as the constituting atoms Rb2 and Si1 are located on the special positions 6*d* and 6*c*, respectively. The polyhedron encircles the smaller dodecahedron (yellow). Twenty-four-atom cages around Rb2 (shown in Figure S1) are omitted in this description of the clathrate-I structure.

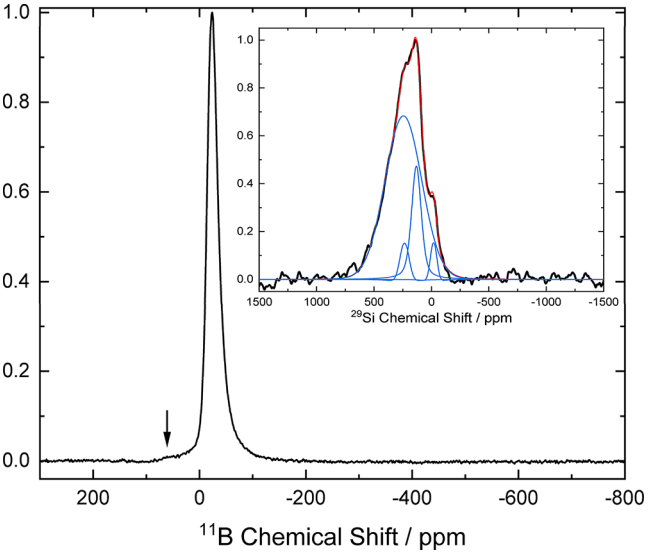

Figure 5. ^{11}B and ^{29}Si NMR spectra of $Rb_8B_8Si_{38}$ at room temperature. Signal at 60 ppm is indicated by an arrow.

semiconductor-like temperature dependence $d\rho/dT < 0$ (Figure 9). The Seebeck coefficient is negative, indicating electrons as dominating charge carriers. As expected, the thermal conductivity of $\kappa(300\ K) = 2\ W\ K^{-1}\ m^{-1}$ is small. The thermoelectric figure of merit $ZT = S^2T\rho^{-1}\kappa^{-1}$ amounts to values close to zero because of the low charge carrier concentration (Zintl limit). The magnetic susceptibility χ of $Rb_8B_8Si_{38}$, measured in the temperature range of 1.8−400 K, denotes diamagnetic behavior and remains constant between

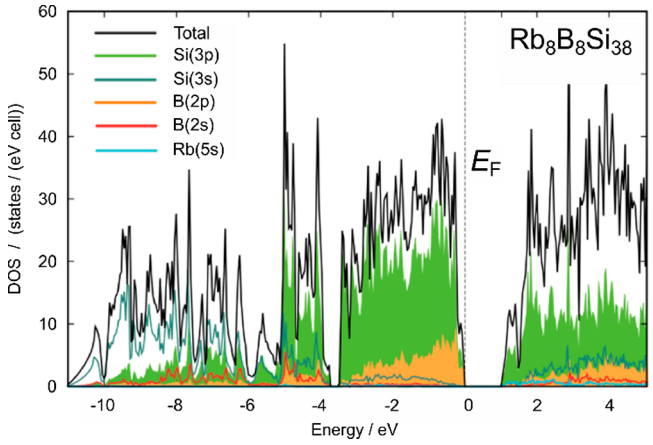

Figure 6. Calculated electronic density of states for an ordered structure model of $Rb_8B_8Si_{38}$ (space group $P\bar{4}3n$).

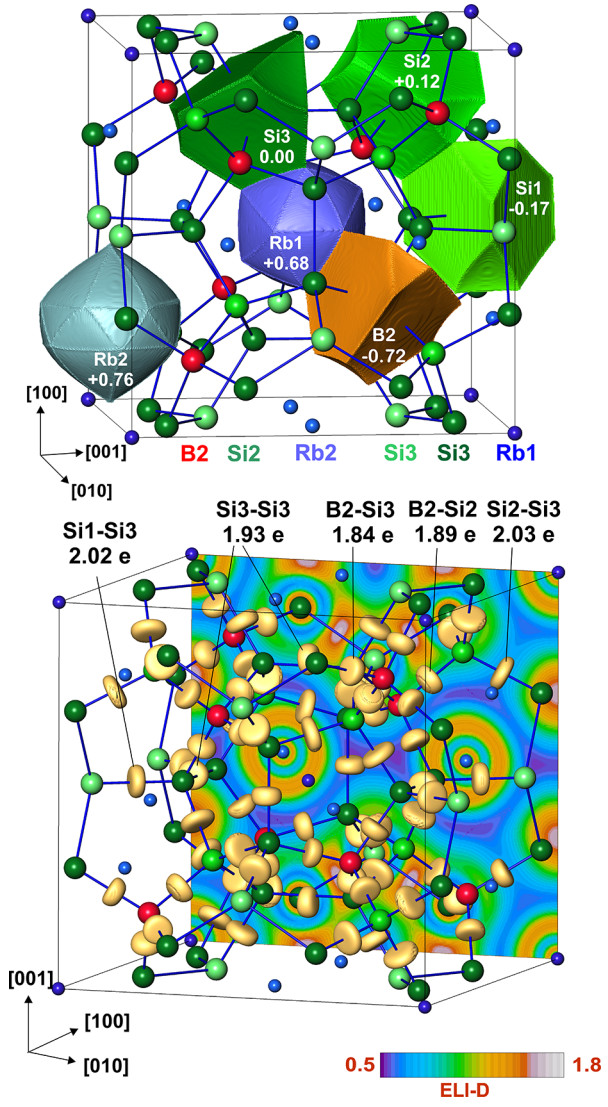

Figure 7. Chemical bonding in $Rb_8B_8Si_{38}$. (Top) Shapes and effective charges of QTAIM atoms visualizing the charge transfer in the structure. (Bottom) Distribution of the electron localizability indicator in the (100) plane and positions of ELI-D maxima shown by the isosurface of ELI-D = 1.6 with the populations of bond basins.

https://dx.doi.org/10.1021/acs.inorgchem.0c02357
Inorg. Chem. 2021, 60, 2160−2167

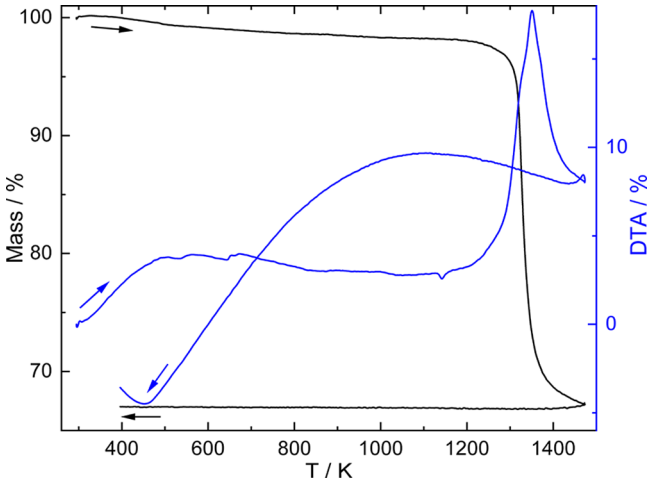

Figure 8. Thermogravimetry (black curve) and differential thermal analysis (blue curve) of $Rb_8B_8Si_{38}$ taken upon heating and cooling in the range 298 K $\leq T \leq$ 1473 K with a heating rate of 10 K min^{-1}.

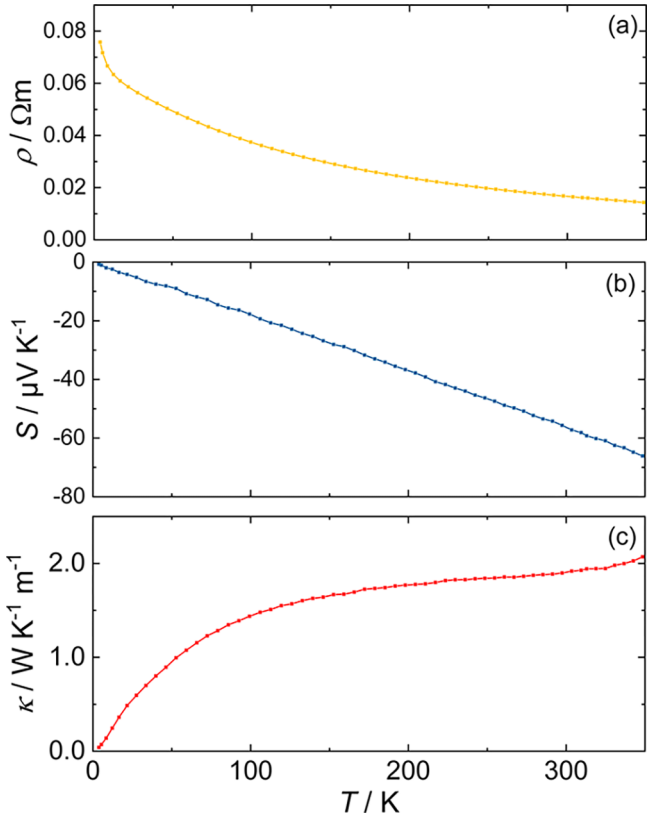

Figure 9. (a) Electrical resistivity $\rho(T)$, (b) Seebeck coefficient $S(T)$, and (c) thermal conductivity $\kappa(T)$ of $Rb_8B_8Si_{38}$.

100 and 400 K (Figure 10). The paramagnetic upturn below 100 K is typical for minor paramagnetic impurity phases. The sum of the diamagnetic increments for Rb^{1+}, B^{3+} and α-Si[47,48] amounts to $\chi = -4.04 \times 10^{-4}$ emu mol^{-1}, which is only slightly smaller than the measured value. Measurements at 0.2 mT did not show any transition into the superconducting state.

4. SUMMARY

The preparation of the new clathrate-I $Rb_8B_8Si_{38}$ underlines the potential of high-pressure synthesis to access new tetrahedral borosilicide frameworks. The description of the

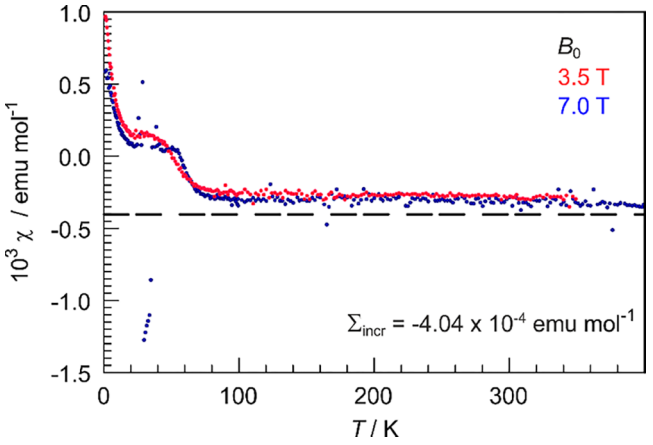

Figure 10. Magnetic susceptibility of $Rb_8B_8Si_{38}$ in the temperature range of 1.8–400 K. The dashed line denotes the sum of the diamagnetic increments.

clathrate-I crystal structure type as a sodalite arrangement enclosing interconnected dodecahedral units emphasizes the separation into a static and a flexible partial structure. The variable part of the clathrate-I crystal structure allows for the specific adaption to various filler and substitution atoms. Analysis of the electron density in $Rb_8B_8Si_{38}$ underlines charges in an anionic clathrate framework of covalently four-bonded Si^0 and B^- following the Zintl model. The chemical bonding is in agreement with the 8-*N* rule and fully consistent with the semiconducting behavior in electronic transport measurements and the calculated electronic density of states. Characterization of the thermoelectric properties reveals acceptable values for thermal conductivity and Seebeck coefficient, but the still significant electrical resistivity requires further optimization by appropriate doping.

■ ASSOCIATED CONTENT

Supporting Information

The Supporting Information is available free of charge at https://pubs.acs.org/doi/10.1021/acs.inorgchem.0c02357.

Additional graphic of the crystal structure and tables with information on data collection, structure refinement and crystallographic data (PDF)

Accession Codes

CCDC 2006313 contains the supplementary crystallographic data for this paper. These data can be obtained free of charge via www.ccdc.cam.ac.uk/data_request/cif, or by emailing data_request@ccdc.cam.ac.uk, or by contacting The Cambridge Crystallographic Data Centre, 12 Union Road, Cambridge CB2 1EZ, UK; fax: +44 1223 336033.

■ AUTHOR INFORMATION

Corresponding Author

Julia-Maria Hübner − *Department of Chemical Metals Science, Max-Planck-Institut für Chemische Physik fester Stoffe, Dresden 01187, Germany*; orcid.org/0000-0003-2048-6629; Email: Julia.Huebner@cpfs.mpg.de

Authors

Walter Jung − *Department of Chemical Metals Science, Max-Planck-Institut für Chemische Physik fester Stoffe, Dresden 01187, Germany*

https://dx.doi.org/10.1021/acs.inorgchem.0c02357
Inorg. Chem. 2021, 60, 2160−2167

Marcus Schmidt − *Department of Chemical Metals Science, Max-Planck-Institut für Chemische Physik fester Stoffe, Dresden 01187, Germany*
Matej Bobnar − *Department of Chemical Metals Science, Max-Planck-Institut für Chemische Physik fester Stoffe, Dresden 01187, Germany*
Primož Koželj − *Department of Chemical Metals Science, Max-Planck-Institut für Chemische Physik fester Stoffe, Dresden 01187, Germany*
Bodo Böhme − *Department of Chemical Metals Science, Max-Planck-Institut für Chemische Physik fester Stoffe, Dresden 01187, Germany;* orcid.org/0000-0003-3102-1130
Michael Baitinger − *Department of Chemical Metals Science, Max-Planck-Institut für Chemische Physik fester Stoffe, Dresden 01187, Germany*
Martin Etter − *Department of Chemical Metals Science, Max-Planck-Institut für Chemische Physik fester Stoffe, Dresden 01187, Germany*
Yuri Grin − *Department of Chemical Metals Science, Max-Planck-Institut für Chemische Physik fester Stoffe, Dresden 01187, Germany;* orcid.org/0000-0003-3891-9584
Ulrich Schwarz − *Department of Chemical Metals Science, Max-Planck-Institut für Chemische Physik fester Stoffe, Dresden 01187, Germany;* orcid.org/0000-0002-7301-8629

Complete contact information is available at: https://pubs.acs.org/10.1021/acs.inorgchem.0c02357

Author Contributions

The manuscript was written through contributions of all authors. All authors have given approval to the final version of the manuscript.

Notes

The authors declare no competing financial interest.

■ ACKNOWLEDGMENTS

We thank Susann Leipe for supporting high-pressure syntheses. We express our gratitude to Ulrich Burkhardt, Sylvia Kostmann, and Petra Scheppan for metallographic analyses. Useful discussions with Frank R. Wagner are gratefully acknowledged. Financial support for J.-M. H. by the International Max Planck Research School for Chemistry and Physics of Quantum Materials (IMPRS-CPQM) is gratefully recognized.

■ REFERENCES

(1) Albert, B.; Hillebrecht, H. Boron: elementary challenge for experimenters and theoreticians. *Angew. Chem., Int. Ed.* **2009**, *48*, 8640−8668.
(2) Lundström, T. Structure, defects and properties of some refractory borides. *Pure Appl. Chem.* **1985**, *57*, 1383−1390.
(3) Mori, T. *Boron-Based Materials. Materials Aspect of Thermoelectricity*; CRC Press; Boca Raton, FL, 2016; Chapter 14, pp 441−457.
(4) Son, H.-W.; Berthebaud, D.; Yubuta, K.; Yoshikawa, A.; Shishido, T.; Suzuta, K.; Mori, T. New Synthesis Route for Complex Borides; Rapid Synthesis of Thermoelectric Yttrium Aluminoboride via Liquid-Phase Assisted Reactive Spark Plasma Sintering. *Sci. Rep.* **2020**, *10*, 8914.
(5) Cherednichenko, K. A.; Mukhanov, V. A.; Wang, Z.; Oganov, A. R.; Kalinko, A.; Dovgaliuk, I.; Solozhenko, V. L. Discovery of new boron-rich chalcogenides: orthorhombic B_6X (X = S, Se). *Sci. Rep.* **2020**, *10*, 9277.
(6) Rasim, K.; Ramlau, R.; Leithe-Jasper, A.; Mori, T.; Burkhardt, U.; Borrmann, H.; Schnelle, W.; Carbogno, C.; Scheffler, M.; Grin, Yu. Local Atomic Arrangements and Band Structure of Boron Carbide. *Angew. Chem., Int. Ed.* **2018**, *57*, 6130−6135.
(7) Akashi, T.; Itoh, T.; Gunjishima, I.; Masumoto, H.; Goto, T. Thermoelectric Properties of Hot-pressed Boron Suboxide (B_6O). *Mater. Trans.* **2002**, *43*, 1719−1723.
(8) Feng, B.; Martin, H. P.; Börner, F. D.; Lippmann, W.; Schreier, M.; Vogel, K.; Lenk, A.; Veremchuk, I.; Dannowski, M.; Richter, C.; Pfeiffer, P.; Zikoridse, G.; Lichte, H.; Grin, Y.; Hurtado, A.; Michaelis, A. Manufacture and Testing of Thermoelectric Modules Consisting of B_xC and TiO_x Elements. *Adv. Eng. Mater.* **2014**, *16*, 1252−1263.
(9) Vojteer, N.; Schroeder, M.; Röhr, C.; Hillebrecht, H. $Li_2B_{12}Si_2$: The First Ternary Compound in the System Li/B/Si: Synthesis, Crystal Structure, Hardness, Spectroscopic Investigations, and Electronic Structure. *Chem. - Eur. J.* **2008**, *14*, 7331−7342.
(10) Zhang, F. X.; Xu, F. F.; Mori, T.; Liu, Q. L.; Tanaka, T. Novel rare-earth borosilicide $RE_{1-x}B_{12}Si_{3.3-\delta}$ (RE = Y, Gd - Lu) ($0 \le x \le 0.5$; $\delta \approx 0.3$): synthesis, crystal growth, structure analysis and properties. *J. Solid State Chem.* **2003**, *170*, 75−81.
(11) Morito, H.; Eck, B.; Dronskowski, R.; Yamane, H. Synthesis and crystal structure of sodium borosilicide, $Na_8B_{74.5}Si_{17.5}$. *Dalton Trans.* **2010**, *39*, 10197−10202.
(12) Jung, W.; Lörincz, J.; Ramlau, R.; Borrmann, H.; Prots, Yu.; Haarmann, F.; Schnelle, W.; Burkhardt, U.; Baitinger, M.; Grin, Yu. $K_7B_7Si_{39}$, a Borosilicide with the Clathrate I Structure. *Angew. Chem., Int. Ed.* **2007**, *46*, 6725−6728.
(13) Dong, Y.; Chai, P.; Beekman, M.; Zeng, X.; Tritt, T. M.; Nolas, G. S. Precursor routes to complex ternary intermetallics: Single-crystal and microcrystalline preparation of clathrate-I $Na_8Al_8Si_{38}$ from NaSi + NaAlSi. *Inorg. Chem.* **2015**, *54*, 5316−5321.
(14) Baran, V.; Senyshyn, A.; Karttunen, A. J.; Fischer, A.; Scherer, W.; Raudaschl-Sieber, G.; Faessler, T. F. A combined metal-halide/metal flux synthetic route towards type-I clathrates: crystal structures and thermoelectric properties of $A_8Al_8Si_{38}$ (A = K, Rb, and Cs). *Chem. - Eur. J.* **2014**, *20*, 15077−15088.
(15) Kroener, R.; Peters, K.; von Schnering, H. G.; Nesper, R. Crystal structure of the clathrates $K_8Ga_8Si_{38}$ and $K_8Ga_8Sn_{38}$. *Z. Kristallogr. NCS* **1998**, *213*, 667−668.
(16) von Schnering, H. G.; Kroener, R.; Menke, H.; Peters, K.; Nesper, R. Crystal structure of the clathrates $Rb_8Ga_8Sn_{38}$, $Rb_8Ga_8Ge_{38}$ and $Rb_8Ga_8Si_{38}$. *Z. Kristallogr. NCS* **1998**, *213*, 677−678.
(17) Baran, V.; Faessler, T. F. Si-based clathrates with partial substitution by Zn and Ga: $K_8Zn_{3.5}Si_{42.5}$, $Rb_{7.9Zn3.6}Si_{42.4}$, and $Cs_{8-x}Ga_{8-y}Si_{38+y}$. *Z. Anorg. Allg. Chem.* **2015**, *641*, 1435−1443.
(18) Zeilinger, M.; van Wüllen, L.; Benson, D.; Kranak, V. F.; Konar, S.; Fässler, T. F.; Häussermann, U. $LiBSi_2$: A Tetrahedral Semiconductor Framework from Boron and Silicon Atoms Bearing Lithium Atoms in the Channels. *Angew. Chem.* **2013**, *125*, 6094−6098.
(19) Cui, X.; Hilleke, K. P.; Wang, X.; Lu, M.; Zhang, M.; Zurek, E.; Li, W.; Zhang, D.; Yan, Y.; Bi, T. RbB_3Si_3: An Alkali Metal Borosilicide that is Metastable and Superconducting at 1 atm. *J. Phys. Chem. C* **2020**, *124* (27), 14826−14831.
(20) Alekseeva, A.; Kovnir, K.; Chizhov, P.; Baitinger, M.; Grin, Yu. Materials purification by treatment with hydrogen-based plasma. Eur. Pat. EP1893320 B8, 2010.
(21) Walker, D.; Carpenter, M. A.; Hitch, C. M. Some simplifications to multianvil devices for high pressure experiments. *Am. Mineral.* **1990**, *75*, 1020−1028.
(22) Akselrud, L.; Grin, Yu. WinCSD: software package for crystallographic calculations (Version 4). *J. Appl. Crystallogr.* **2014**, *47*, 803−805.
(23) Koepernik, K.; Eschrig, H. Full-potential nonorthogonal local-orbital minimum-basis band-structure scheme. *Phys. Rev. B: Condens. Matter Mater. Phys.* **1999**, *59*, 1743−1757.
(24) Perdew, J. P.; Wang, Y. Accurate and simple analytic representation of the electron-gas correlation energy. *Phys. Rev. B: Condens. Matter Mater. Phys.* **1992**, *45*, 13244.
(25) Bader, R. F. W. *Atoms in Molecules—A Quantum Theory*; Clarendon Press, Oxford, U.K., 1995.

(26) Kohout, M. A measure of electron localizability. *Int. J. Quantum Chem.* **2004**, *97*, 651−658.
(27) (a) Kohout, M.; Wagner, F. R.; Grin, Y. Atomic shells from the electron localizability in momentum space. *Int. J. Quantum Chem.* **2006**, *106*, 1499−1507. (b) Kohout, M. Bonding indicators from electron pair density functionals. *Faraday Discuss.* **2007**, *135*, 43−54.
(28) Ormeci, A.; Rosner, H.; Wagner, F. R.; Kohout, M.; Grin, Yu. Electron localization function in full-potential representation for crystalline materials. *J. Phys. Chem. A* **2006**, *110*, 1100−1105.
(29) Kohout, M. *DGRID*, Version 4.6; Radebeul, Germany, 2011.
(30) Kasper, J.; Hagenmuller, P.; Pouchard, M.; Cros, C. Clathrate Structure of Silicon Na_8Si_{46} and Na_xSi_{136} ($x < 11$). *Science* **1965**, *150*, 1713−1714.
(31) Stefanoski, S.; Nolas, G. S. Synthesis and Structural Characterization of Single-Crystal $K_{7.5}Si_{46}$ and $K_{17.8Si136}$ Clathrates. *Cryst. Growth Des.* **2011**, *11*, 4533−4537.
(32) Ramachandran, G. K.; McMillan, P. F.; Dong, J.; Sankey, O. F. $K_{7.62(1)}Si_{46}$ and $Rb_{6.15(2)}Si_{46}$: Two Structure I Clathrates with Fully Occupied Framework Sites. *J. Solid State Chem.* **2000**, *154*, 626−634.
(33) Veremchuk, I.; Beekman, M.; Antonyshyn, I.; Schnelle, W.; Baitinger, M.; Nolas, G. S.; Grin, Yu. Binary Alkali-Metal Silicon Clathrates by Spark Plasma Sintering: Preparation and Characterization. *Materials* **2016**, *9*, 593.
(34) Dolyniuk, J. A.; Owens-Baird, B.; Wang, J.; Zaikina, J. V.; Kovnir, K. Clathrate thermoelectrics. *Mater. Sci. Eng., R* **2016**, *R108*, 1−46.
(35) Cros, C.; Pouchard, M. Sur les phases de type clathrate du silicium et des éléments apparentés (C, Ge, Sn): Une approche historique. *C. R. Chim.* **2009**, *12*, 1014−1056.
(36) Bohme, B.; Guloy, A.; Tang, Z.; Schnelle, W.; Burkhardt, U.; Baitinger, M.; Grin, Y. Oxidation of M_4Si_4 (M = Na, K) to Clathrates by HCl or H_2O. *J. Am. Chem. Soc.* **2007**, *129*, 5348−5349.
(37) Ramachandran, G. K; Dong, J.; Diefenbacher, J.; Gryko, J.; Marzke, R. F; Sankey, O. F; McMillan, P. F Synthesis and X-ray characterization of silicon clathrates. *J. Solid State Chem.* **1999**, *145*, 716−730.
(38) Stefanoski, S.; Nolas, G. S. Synthesis and structural characterization of single-crystal $K_{7.5}Si_{46}$ and $K_{17.8}Si_{136}$ clathrates. *Cryst. Growth Des.* **2011**, *11*, 4533−4537.
(39) Gallmeier, J.; Schäfer, H.; Weiss, A. K_8Si_{46}, ein Silicid mit Käfigstruktur. *Z. Naturforsch., B: J. Chem. Sci.* **1967**, *22*, 1080.
(40) Wosylus, A.; Veremchuk, I.; Schnelle, W.; Baitinger, M.; Schwarz, U.; Grin, Yu. $Cs_{8-x}Si_{46}$: A type-I clathrate with expanded silicon framework. *Chem. - Eur. J.* **2009**, *15*, 5901−5903.
(41) Jaussaud, N.; Pouchard, M.; Goglio, G.; Cros, C.; Ammar, A.; Weill, F.; Gravereau, P. High pressure synthesis and structure of a novel clathrate-type compound: $Te_{7+x}Si_{20-x}$ ($x \sim 2.5$). *Solid State Sci.* **2003**, *5*, 1193−1200.
(42) Bobnar, M.; Böhme, B.; Wedel, M.; Burkhardt, U.; Ormeci, A.; Prots, Yu.; Drathen, C.; Liang, Y.; Nguyen, H. D.; Baitinger, M.; Grin, Yu. Distribution of Al atoms in the clathrate-I phase $Ba_8Al_xSi_{46-x}$ at x = 6.9. *Dalton Trans.* **2015**, *44*, 12680−12687.
(43) Structure model of $Rb_8B_8Si_{38}$ used as input for QTAIM charge calculations: space group $P\bar{4}3n$; a = 9.9583 Å; Rb1 at 2*a*, 0 0 0; Rb2 at 6*c*, 1/4 1/2 0; Si1 at 6*d*, 1/4 0 1/2; Si2 at 8*e*, 0.1912 *x x*; B2 at 8*e*, 0.3188 *x x*; Si3 at 24*i*, 0 0.2973 0.1243.
(44) Castillo, R.; Schnelle, W.; Bobnar, M.; Burkhardt, U.; Böhme, B.; Baitinger, M.; Schwarz, U.; Grin, Yu. The Clathrate $Ba_{8-x}Si_{46}$ Revisited: Preparation Routes, Electrical and Thermal Transport Properties. *Z. Anorg. Allg. Chem.* **2015**, *641*, 206−213.
(45) Hübner, J.-M.; Prots, Yu.; Schnelle, W.; Bobnar, M.; König, M.; Baitinger, M.; Simon, P.; Carrillo-Cabrera, W.; Ormeci, A.; Svanidze, E.; Grin, Yu.; Schwarz, U. In-Cage Interactions in the Clathrate Superconductor Sr_8Si_{46}. *Chem. - Eur. J.* **2020**, *26*, 830−838.
(46) Lide, D. R. *CRC Handbook of Chemistry and Physics: A Ready-Reference Book of Chemical and Physical Data*. 87th ed.; CRC Taylor & Francis; Boca Raton, FL, 2006.
(47) Selwood, P. W. *Magnetochemistry*; Interscience: New York, 2nd ed., 1956; p 78.
(48) Hudgens, S.; Kastner, M.; Fritzsche, H. Diamagnetic Susceptibility of Tetrahedral Semiconductors. *Phys. Rev. Lett.* **1974**, *33*, 1552−1555.

https://dx.doi.org/10.1021/acs.inorgchem.0c02357
Inorg. Chem. 2021, 60, 2160−2167